# Tunneling optoresistance effect in two-dimensional modulated quantum structures

Sheng-Xiang Wang, Lai-Peng Luo, and Yong Guo*

*Department of Physics and State Key Laboratory of Low-Dimensional Quantum Physics, Tsinghua University, Beijing 100084, People's Republic of China*

(Received 8 July 2023; revised 10 January 2024; accepted 1 February 2024; published 21 February 2024)

Spin- and valley-resolved transport properties of a double beam off-resonant circular polarized light-modulated (CPL-modulated) junction based on monolayer transition-metal dichalcogenides (TMDc) are studied. We find that tuning between a high resistance configuration and a low resistance one can be realized with pure CPL modulation. Numerical results of spin- and valley-resolved transport show the tunneling resistance induced by CPL is different from previously reported tunneling magnetoresistance (TMR) effect based on two-dimensional materials. Out of analogy, we name it as the tunneling optoresistance (TOR) effect, and introduced TOR ratio to depict the difference between configurations with high and low tunneling resistance. Our results imply that $\mathrm{TOR}_{\max} = 1$ can be realized when the CPL-induced gap is beyond a certain limit. We also give an intuitive explanation under near the $K/K'$ valley approximation which matches numerical results well. Our results show optically modulated quantum structures based on TMDc materials may dynamically tune between a high resistance configuration and a low resistance configuration, indicating its promising potential for applications in high-speed storage and spintronic or valleytronic devices.

DOI: 10.1103/PhysRevB.109.085131

## I. INTRODUCTION

In recent years, optoelectronic and spintronic devices have attracted substantial attention due to their potential for high-density information storage and low-power computing [1–4]. Monolayer transition-metal dichalcogenides (TMDc) are a family of two-dimensional (2D) materials in the form of $\mathbf{MX_2}$, where one transition metal atom ($\mathbf{M}$ = Mo, W, etc.) is sandwiched between two chalcogen atoms ($\mathbf{X}$ = S, Se, Te, etc.). Several materials in the family of monolayer TMDc, such as monolayer molybdenum disulfide ($MoS_2$) [5,6], monolayer tungsten diselenide ($WSe_2$) [7,8], and monolayer molybdenum diselenide ($MoSe_2$) [9,10] have been synthesized recently. Monolayer TMDc have a large direct band gap and strong spin-orbit coupling (SOC), thus they are appropriate candidates in the research of spintronics and valleytronics [11–19]. Similar to graphene, the conduction and valence-band edges of monolayer TMDc are located at the corners (K points) of the first hexagonal Brillouin zone. Thus, low-energy carriers are assigned a new index by the two inequivalent valleys $K$ and $K'$. Two important distinctions between TMDc and graphene are the inherently broken inversion symmetry and strong SOC. These two distinctions lead to the spin-valley locking phenomena [20]: the spin-splitting of the valence band is opposite at the two valleys, which is required by time-reversal symmetry [21,22].

The tunneling magnetoresistance (TMR) effect [23,24] is a promising topic that has been extensively studied, which has obtained applications in storage and computing devices such as magnetic random access memory (MRAM) [25] and hard disk drives (HDDs) [26]. The TMR effect is concerned with the electrically controlled charge switch under different magnetizations. Based on 2D materials (i.e., graphene, silicene, phosphorene, etc.), several practical symmetric junctions that produce the TMR effect have been proposed [27–38]. Especially, owing to the broken inversion symmetry, optical pumping is introduced as an approach to obtain valley polarization in several works based on monolayer TMDc. In a ferromagnetic-ferromagnetic-normal (FFN) $MoS_2$ tunnel junction, asymmetrical magnetization and the valley degeneracy breaking of off-resonant light causes spin imbalance, thus spin-valley filtering is achieved [39]. In a study of magnetoresistance in asymmetric ferromagnetic $WSe_2$ tunnel junctions [35], spin and valley polarizations are found to be tunable and switchable in the presence of an off-resonant circular polarized light (CPL), and TMR can be tuned to one. Compared with applying strain or magnetic fields, the approach of optical pumping with CPL allows dynamic control compared with applying strain or magnetic fields, and its viability has been demonstrated experimentally [40,41].

While the approach of optical pumping is no longer novel in searching for the possibility of valley-based electronic applications, the tunneling resistance caused by the purely optical Stark effect has never been studied. In fact, by utilizing the valley switch under different helicity of light, an effect in the same magnitude with the TMR effect can be achieved based on TMDc materials, without the involvement of the magnetic field. Inspired by research on magnetoresistance, we studied a pure CPL-modulated junction, which resembles previous studied ferromagnetic-normal-ferromagnetic (FNF) junction [42]. We find tunneling resistance can be induced by switching between parallel and antiparallel configurations of CPL. Such an effect is named the tunneling optoresistance (TOR) effect, which resembles the TMR effect.

*Corresponding author: guoy66@tsinghua.edu.cn

 

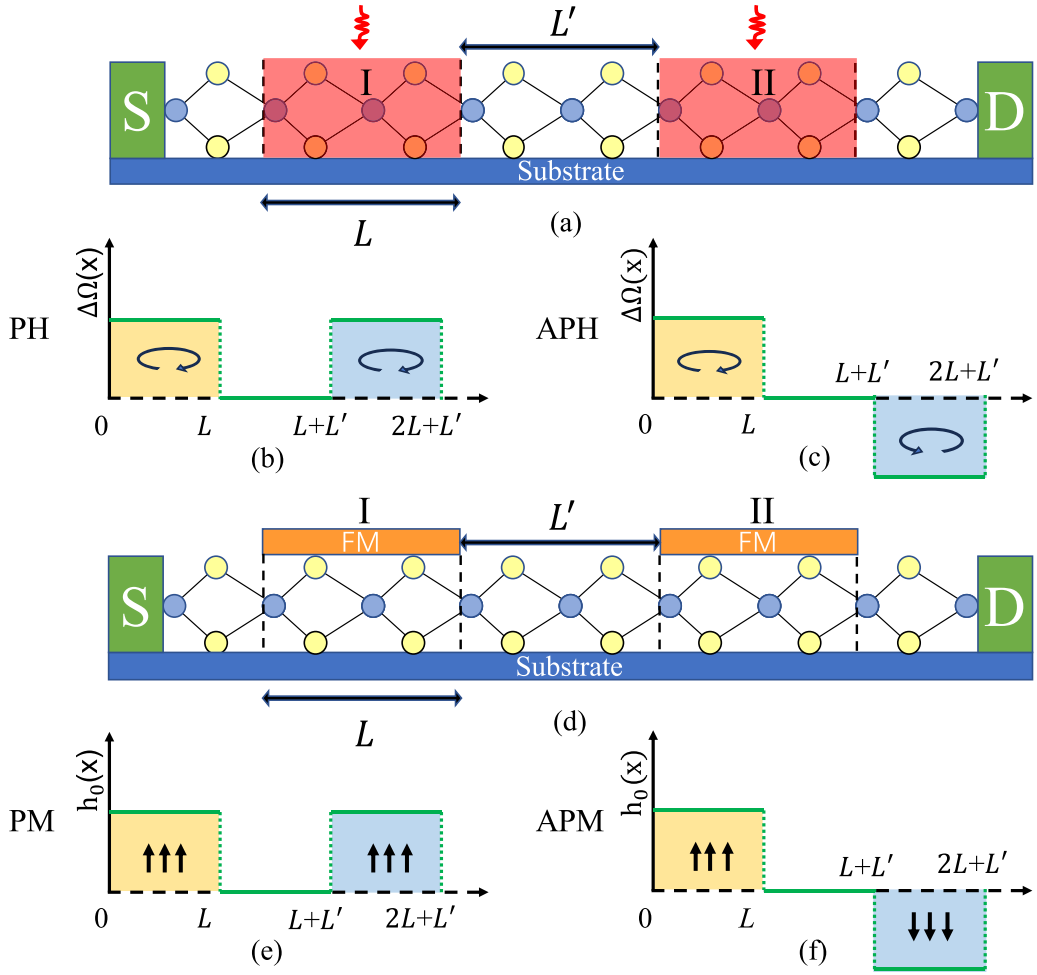


FIG. 1. (a) Schematic diagram of a CPL-modulated 2D quantum structure, (b) CPL-induced gap in PH configuration, and (c) APH configuration. (d) Schematic diagram of an FNF junction, (e) exchange splitting in PM configuration, and (f) APM configuration.

## II. MODEL AND METHODS

The schematic diagram of our proposed model is shown in Fig. 1(a). The CPL-modulated regions are of the same width $L$. The central region is unmodulated, with the width of $L'$. The electromagnetic potential of CPL can be described by vector $\boldsymbol{A}(t) = [A_0 \sin(\pm\Omega t), A_0 \cos(\pm\Omega t)]$, where $A_0$ is the amplitude of potential and $\Omega$ is the frequency. When the CPL illuminated on regions is off resonance, which requires $\hbar|\Omega| \gg \tau$ ($\tau$ is the nearest-neighbor hopping parameter), the electron band gap is modified by virtual photon absorption process. According to Floquet theory [43,44], off-resonance CPL interacts with carriers by second-order virtual photon absorption processes, which can be depicted by an effective static Hamiltonian. For $eA_0 v_f/\hbar\Omega \ll 1$, the effective Hamiltonian near the Dirac point can be written as

$$H = \hbar v_f(k_x\hat{\eta}_z\hat{\sigma}_x + k_y\hat{\sigma}_y) + [\Delta \pm \Delta\Omega(x)\hat{\eta}_z]\hat{\sigma}_z + \hat{\eta}_z\hat{s}_z\lambda_v(\hat{\sigma}_0 - \hat{\sigma}_z), \quad (1)$$

where $\hat{s}_i$, $\hat{\eta}_i$, and $\hat{\sigma}_i$ are Pauli matrices for spin, valley, and sublattice pseudospin spaces ($\hat{\sigma}_0$ is identity matrix for the sublattice space), $v_f$ is the Fermi velocity, $\Delta$ is half of the band gap, and $4\lambda_v$ is the spin splitting on the valence band caused by the SOC. The sign $\pm$ corresponds to the right-handed and left-handed CPL in region I. The CPL-induced gap $\Delta\Omega(x) = \Delta\Omega_0[\Theta(x)\Theta(L-x) \pm \Theta(x-(L+L'))\Theta(2L+L'-x)]$, where $\Theta(x)$ is the Heaviside step function, and $\Delta\Omega_0 = (eA_0 v_f)^2/\hbar\Omega_0$. Here, the sign $\pm$ corresponds to two configurations: parallel helicity (PH) and antiparallel helicity (APH) [see Figs. 1(b) and 1(c)]. Note that the CPL-induced band gap in regions I and II is set to be the same in this work, since we only focus on the difference between configurations. Different CPL-induced band gaps in regions I and II will bring further differences in the same configuration, which is beyond our discussion here.

Here, we design and compare two configurations of junction: the parallel helicity (PH) configuration and antiparallel helicity (APH) one. In the PH configuration, CPL in regions I and II are with the same helicity, while in the APH configuration, CPL in regions I and II have opposite helicity, i.e., $\Delta\Omega_I = -\Delta\Omega_{II} = \Delta\Omega_0 = (eAv_f)^2/\hbar\Omega_0$.

Assuming $k_j$ is the wave vector in the $j$th region, due to the translational invariance in the $y$ direction, we have a conserved transverse wave vector $k_y$. By boundary conditions, it is easily resolved that $k_y$ is identical for all regions. The wave function

in region $j$ can be written as

$$\psi_j(x) = A_j \begin{pmatrix} 1 \\ v_{j,+} \end{pmatrix} e^{ik_{x,j}x+ik_y y} + B_j \begin{pmatrix} 1 \\ v_{j,-} \end{pmatrix} e^{-ik_{x,j}x+ik_y y}. \quad (2)$$

By solving the energy eigenequation, we obtain the vector coefficients $v_{j,\pm}$:

$$v_{j,\pm} = \frac{\hbar v_F(\pm\eta_z k_{x,j} + ik_y)}{\Delta + \eta_z \Delta\Omega(x) + E_j - 2\eta_z s_z \lambda_v}. \quad (3)$$

where $\eta_z = \pm 1$ corresponds to the valleys $K$ and $K'$, $s_z = \pm 1$ represents spin up and spin down. In region $j$, the longitudinal wave vector $k_{x,j}$ is correlated to carrier energy $E_j$ as

$$k_{x,j}^2 = [\Delta + \eta_z \Delta\Omega(x) - E_j][-\Delta - \eta_z \Delta\Omega(x) - E_j + 2\eta_z s_z \lambda_v]/(\hbar v_F)^2 - k_y^2. \quad (4)$$

For comparison, a magnetically modulated model—ferromagnetic-normal-ferromagnetic (FNF) junction—based on TMDc is also considered [see Fig. 1(d)]. The effective Hamiltonian near the Dirac point is given as

$$H = \hbar v_f(\hat{\eta}_z k_x \hat{\sigma}_x + k_y \hat{\sigma}_y) + \Delta\hat{\sigma}_z + \hat{\eta}_z \hat{s}_z \lambda_v(\hat{\sigma}_0 - \hat{\sigma}_z) - \hat{s}_z h(x). \quad (5)$$

The exchange splitting induced by ferromagnetic regions $h(x)$ can be described through the Heaviside step function: $h(x) = h_0[\Theta(x)\Theta(L-x) \pm \Theta(x-(L+L'))\Theta(2L+L'-x)]$. Similar to the CPL modulated case, $\pm$ corresponds to two configurations: parallel magnetization (PM) and antiparallel magnetization (APM) [see Figs. 1(e) and 1(f)].

In this work, the transfer matrix method is used to solve the spin- and valley-resolved transmission $T_{\eta_z,s_z}(E_0,\theta_0)$, where $E_0$ stands for the incident energy, measured from the energy of the Dirac point, and $\theta_0$ is the incident angle. The spin-valley-resolved conductance is given by the Landauer-Büttiker theory [45]:

$$G_{\eta_z,s_z}(E_F) = G_0 \int_{-\pi/2}^{\pi/2} T_{\eta_z,s_z}(E_F,\theta_0)\cos\theta_0 d\theta_0, \quad (6)$$

where $G_0 = e^2 L_y E_F/(2\pi\hbar h v_F)$ is the conductance-reduced unit with the system transverse length $L_y$ and $E_F$ is the Fermi energy.

The spin-resolved conductance and valley-resolved conductance, $G_{\uparrow(\downarrow)}$, $G_{\eta,\uparrow(\downarrow)}$, are defined as

$$G_{\uparrow(\downarrow)} = \sum_\eta G_{\eta,\uparrow(\downarrow)}, \quad (7)$$

$$G_{K(K')} = \sum_{s_z} G_{K(K'),s_z}. \quad (8)$$

The total conductance is defined as

$$G_{\text{total}} = \sum_{\eta,s_z} G_{\eta,s_z}. \quad (9)$$

To distinguish between the CPL-modulated and magnetically modulated cases, total conductances are further labeled as $G_{\text{total}}^{\text{PH}}$ and $G_{\text{total}}^{\text{APH}}$ for the PH and APH configurations, as $G_{\text{total}}^{\text{PM}}$ and $G_{\text{total}}^{\text{APM}}$ for the PM and APM configurations.

## III. NUMERICAL RESULTS AND DISCUSSION

First, we show and compare the transport properties of a FNF junction with our proposed optically modulated quantum structure. Without losing generality, we choose material parameters of monolayer $MoS_2$ for concrete numerical calculation throughout this work: $\tau = 1.10$ eV, $v_f = 5.3 \times 10^5$ m s$^{-1}$, $\Delta = 0.833$ eV, and $4\lambda_v = 150$ meV. For the validity of our model, width of each regions are set as $L = L' = 5$ nm.

In the magnetically modulated case, we set $h_0 = 100$ meV and consider only the case of normal incidence, which means $\theta_0 = 0°$. The spin-dependent term $s_z h(x)$ contributes to main difference when we traverse all spin and valley indices, since $\lambda_v$ is significantly smaller than $h_0$. As a result, we find major differences between the transmission of spin-up and spin-down electrons. In the PM configuration [see Figs. 2(a) and 2(b)], line-type resonant tunneling peaks appear with tiny energy shifts for $K\uparrow$ and $K'\uparrow$ electrons. These resonant tunneling peaks derive from barriers of magnetic effective potentials brought by term $s_z h(x)$. Quasibound states are formed in the unmodulated region between regions I and II. Resonant tunneling occurs when the energy of tunneling carriers is exactly the same with discrete quasibound levels. However, for spin-down electrons, $s_z h(x)$ is negative in modulated regions, forming potential wells rather than barriers. Thus the transmission is enhanced and no resonant peaks show up. The significant difference in the transmission spectra of different spins vanishes in the APM configuration [see Figs. 2(c) and 2(d)]. This peculiarity is attributed to the $\eta s$ degeneracy in the APM configuration. When the sign of $\eta$ and $s$ are both reversed, the Hamiltonian can still be kept invariant by flipping the signs of $k_x$ and $h(x)$ correspondingly. In this case, the new Hamiltonian depicts a right-to-left transmission process, where the direction of magnetic exchange field in both modulated regions are reversed. In the APM configuration, the new potential function acquired after flipping signs is identical with the original one, therefore transmission channels with the same $\eta s$ value are degenerate. Such degeneracy requires the same transmission after flipping only the spin or valley index, thus the transmission difference between opposite spins and valleys is also restricted to be the same.

For comparison, we set $\Delta\Omega_0 = 100$ meV, $\theta_0 = 0°$ in the CPL-modulated case. Calculation of the conduction-band energy using Eq. (4) shows that, when $k$ is much smaller than $\Delta/(\hbar v_F)$, the energy shift can be approximately as $\Delta E \approx \lambda_v k^2/[(\Delta + \eta\Delta\Omega)^2 - \lambda_v^2]$, which is a small energy at the level of $k^2\lambda_v/\Delta^2$. This result is particularly evident in the small energy shift of linear resonance peaks of K spin up and down shown in Figs. 2(e) and 2(g). In the contrast, valley-dependent term $\Delta\Omega(x)\hat{\eta}_z\hat{\sigma}_z$ contributes to main difference between the Hamiltonian for spins and valleys, making the transmission for $K$ and $K'$ valleys significantly different [see Figs. 2(e)–2(h)]. For the $K$ valley, ideal line-type resonant tunneling peaks appear in the PH configuration [see Fig. 2(e)]. Distinct from the magnetic modulated case, CPL-induced term $\Delta\Omega(x)\hat{\eta}_z\hat{\sigma}_z$ changes band gap rather than lift or lower band energy. When CPL is right-hand polarized, the band gap is enlarged for the $K$ valley potential. As a result, in PH configuration the conduction-band energy is raised in both

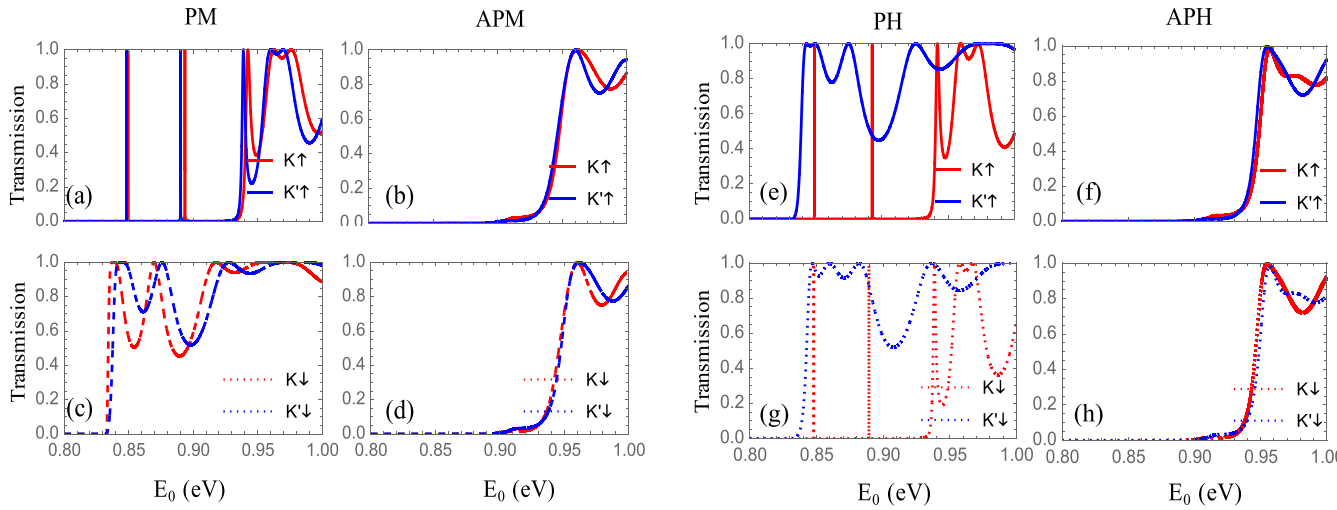


FIG. 2. (a)–(d) Spin- and valley-resolved transmission in 2D magnetically modulated quantum structures at $h_0 = 100$ meV. (a), (b): In the PM configuration; (c), (d): in the APM configuration. (e)–(h) Spin- and valley-resolved transmission in 2D CPL-modulated quantum structures at $\Delta\Omega_l = 100$ meV. (e), (f) In the PH configuration, (g), (h) in the APH configuration.

modulated regions, forming potential barriers in the conduction band. Similar to the case of magnetically modulation, quasibound states are formed in the central region of the optically modulated structure, which explains the appearance of ideal line-type resonant tunneling peaks. For $K'$ valley particles, the band gap is narrowed in both modulated regions, forming two potential wells in the conduction band. Transmission is enhanced in such cases, and no line-type resonant tunneling peaks can be observed [see Fig. 2(f)]. In the APM configuration, owing to $\eta s$ degeneracy, the difference between the transmission of spin up and down, valley $K$ and $K'$ is still restricted as in the magnetically modulated case.

Figure 3 displays a color map of the CPL-modulated transmission as a function of $\Delta\Omega_0$ and incident angle $\theta_0$. The Fermi energy is set as a constant $E_F = 1.5\Delta$ in the following discussion. The value of transmission probability ranges from zero (blue) to one (red). Zero and one indicate total reflection and ideal transmission, respectively. Perfect transmission zones colored with red are dominant when $\Delta\Omega_0$ is close to zero. As $\Delta\Omega_0$ increases, total transmission zones shrink towards low incident angles, and the highest $\Delta\Omega_0$ in transmission zones correspond to $\theta_0 = 0$. In the PH configuration, the transmission for $K$ valley is completely blocked when $\Delta\Omega_0$ is above $0.5\Delta$ [see Figs. 3(a) and 3(b)], while for the $K'$ valley, total transmission can still be achieved with $\Delta\Omega_0 > \Delta$ around certain $\theta_0$. In the APH configuration, the transmission for $K$ and $K'$ valleys are both blocked when $\Delta\Omega_0 > 0.5\Delta$. Moreover, the transmission zones of $K\uparrow$, $K\downarrow$, $K'\uparrow$, and $K'\downarrow$ are almost consistent, which verifies the $\eta s$ degeneracy rule once again.

The spin- and valley-resolved conductances with respect to Fermi energy in magnetic modulated and CPL-modulated quantum structures are shown in Fig. 4. For FNF magnetic junctions, $G_\downarrow$ is significantly higher than $G_\uparrow$ in the PM configuration, especially with low Fermi energy. Still, a tiny difference can be observed between the conductance of $K$ and $K'$ valleys. In the APM configuration, spin polarization and valley polarization are tiny because of $\eta s$ degeneracy, which is a repetition of transmission results discussed in Fig. 2.

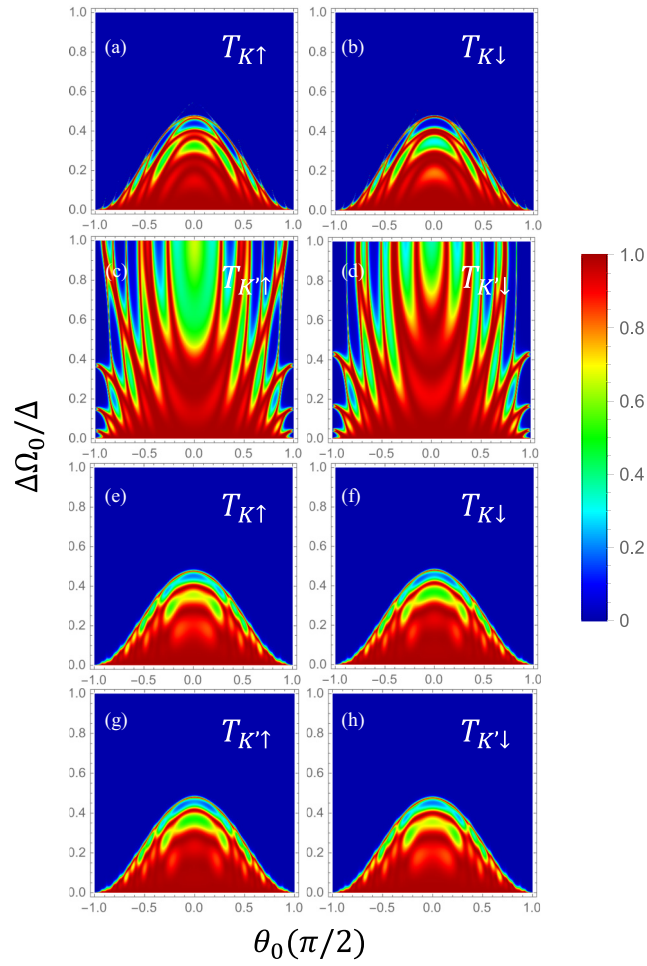


FIG. 3. Transmission maps as a function of $\Delta\Omega_0$ and incident angle $\theta_0$, in CPL-modulated quantum structures. (a)–(d) Transmission maps for the PH configuration. (e)–(h) Transmission maps for the APH configurations. The parameters here are $E_0 = 1.5\Delta$ and $L = 5$ nm.

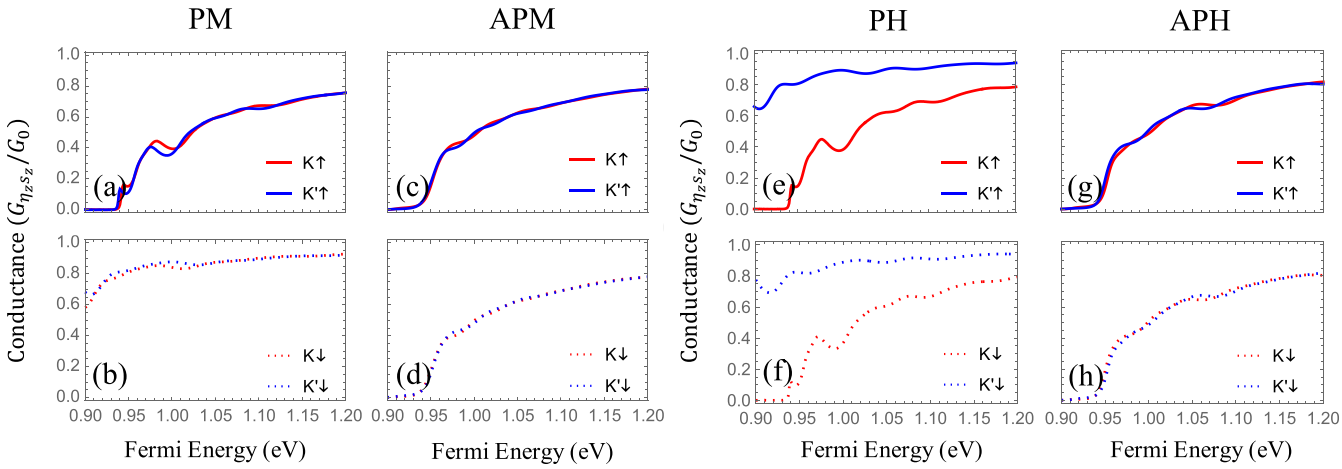


FIG. 4. (a)–(d) Spin- and valley-resolved conductance with respect to Fermi energy, in magnetically modulated quantum structures, $m_0 = 100$ meV. (a), (b) PM configuration. (c), (d) APM configuration. (e)–(h) Spin- and valley-resolved transmission in 2D CPL-modulated quantum structures, at $\Delta\Omega_I = 100$ meV. (e), (f) In the PH configuration. (g), (h) In the APH configuration.

For CPL-modulated structures, $G_{K'}$ is significantly larger than $G_K$ in the PH configuration. With $E_F$ lower than 0.93 eV [see Figs. 4(e) and 4(f)], $G_K$ is close to zero, while $G_{K'}$ is still considerable, thus the conductance is close to fully K polarized. The consequence that $G_{K'}$ is higher in the PH configuration than in the APH configuration can also be indicated by the high transmission of $K'$ valley beyond $0.5\Delta$ in the PH configuration [see Fig. 3]. In contrast, both $G_K$ and $G_{K'}$ are close to zero when $E_F$ is lower than 0.93 eV in the APH configuration [see Figs. 4(g) and 4(h)]. Moreover, both the spin and valley polarization are very weak for any Fermi energy due to the existence of $\eta s$ degeneracy.

We show the total conductance with respect to modulation parameters in Fig. 5. Obviously, for both magnetically modulated and CPL-modulated cases, the difference between total conductance of parallel and antiparallel configurations is enlarged under stronger modulation [see Figs. 5(a) and 5(c)]. In CPL-modulated structures, total conductance for the APH configuration ($G^{\mathrm{APH}}_{\mathrm{total}}$) rapidly decays to zero as $|\Delta\Omega_0|$ increases. For the PH configuration, a rather small decay rate of total conductance ($G^{\mathrm{PH}}_{\mathrm{total}}$) is observed when $\Delta\Omega_0/\Delta$ approaches one. Furthermore, The decay rate of $G_{\mathrm{total}}$ in either configuration declines significantly as $E_F$ varies from 1.1 to 1.5 eV. These results are completely consistent with the case of magnetic modulation.

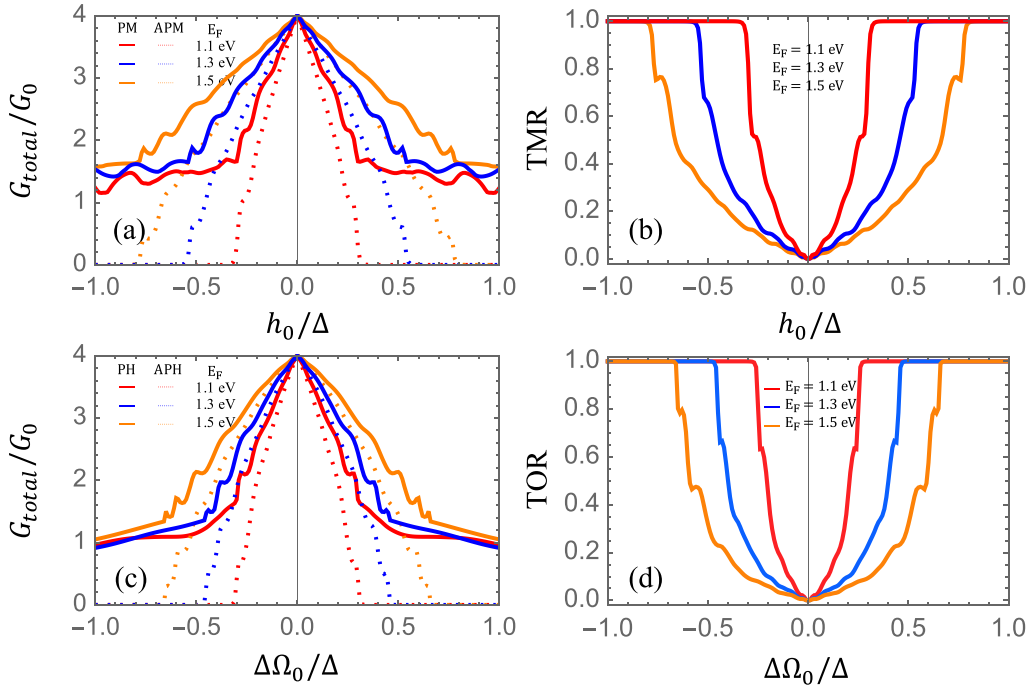


FIG. 5. (a) $G_{\mathrm{total}}/G_0$ and (b) TMR with respect to $h_0$ in 2D magnetically modulated quantum structures. (c) $G_{\mathrm{total}}/G_0$ and (d) TOR with respect to $\Delta\Omega_0$ in 2D CPL-modulated quantum structures.

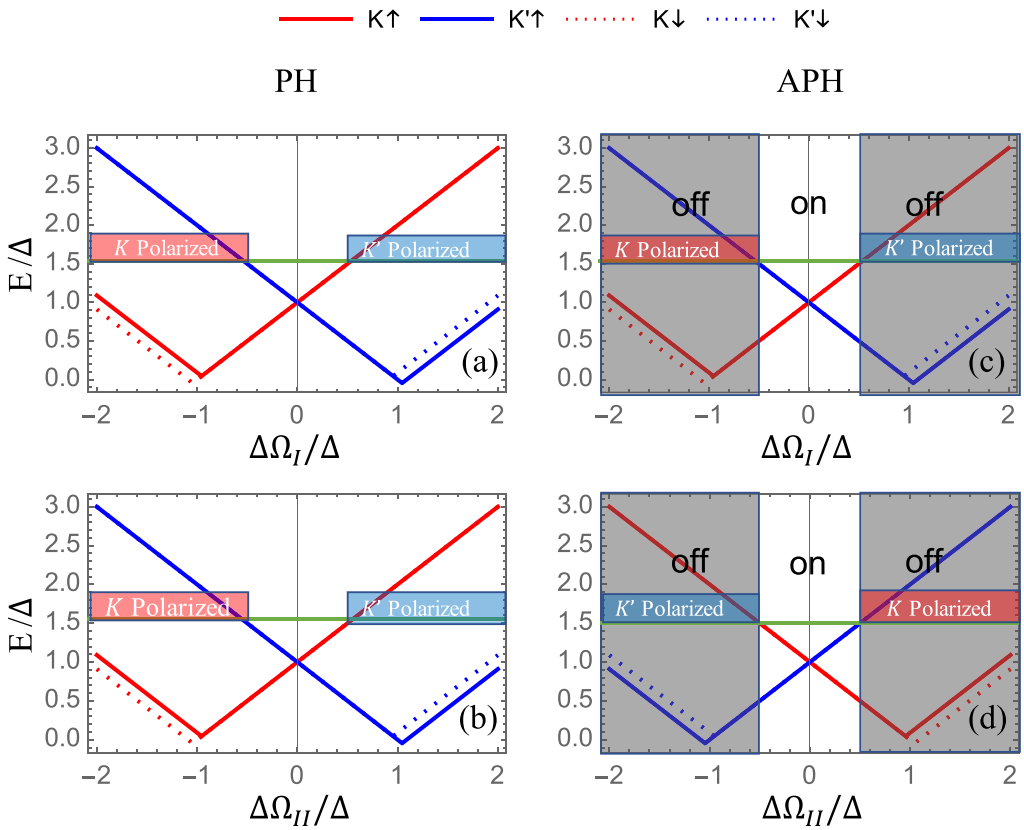


FIG. 6. The effective conduction-band energy near the $K$ and $K'$ valleys with respect to the CPL-induced gap in each CPL modulated region. (a), (b) PH configuration. (c), (d) APH configuration.

For 2D magnetic junctions, difference between the total conductance of PM configuration and APM configuration is usually depicted by the TMR ratio as follows:

$$\mathrm{TMR} = \frac{G^{\mathrm{PM}}_{\mathrm{total}} - G^{\mathrm{APM}}_{\mathrm{total}}}{G^{\mathrm{PM}}_{\mathrm{total}}}. \tag{10}$$

Correspondingly, we introduce the tunneling optoresistance (TOR) ratio to depict the difference between the total conductance of PH configuration and APH configuration:

$$\mathrm{TOR} = \frac{G^{\mathrm{PH}}_{\mathrm{total}} - G^{\mathrm{APH}}_{\mathrm{total}}}{G^{\mathrm{PH}}_{\mathrm{total}}}. \tag{11}$$

Note that higher TOR represents more significant relative difference between total conductance of the PH configuration and the APH configuration.

Figure 5(d) shows the calculated TOR with respect to $\Delta\Omega_0$ at different $E_F$. At $E_F = 1.1$ eV, TOR increases from zero to one with $\Delta\Omega_0/\Delta \approx 0.3$, while $\Delta\Omega_0/\Delta \approx 0.7$ is required for $\mathrm{TOR} = 1$ at $E_F = 1.5$ eV. As we discussed above, in CPL-modulated models $G_{K'}$ in the PH configuration is significantly larger than $G_K$, along with $G_K$, $G_{K'}$ in the APH configuration [see Fig. 3]. When $\Delta\Omega_0/\Delta$ is sufficiently large, the electronic transport in the APH configuration is completely blocked, which results in $\mathrm{TOR} = 1$.

In general cases, the limit of $\Delta\Omega_0$ which can induce 100% TOR differs in each type of TMDc materials. We may roughly evaluate this limit by analyzing the effective conduction energy bands near the $K$ and $K'$ valleys. To give a clear interpretation of each valley's contribution to total conductance, the conduction-band energy near the $K$ and $K'$ valleys in CPL-modulated regions is shown in Fig. 6. If both $K$ and $K'$ valleys contribute to electronic transport in the CPL-modulated region, $E_F - \eta s\lambda_v > |\Delta + \eta\Delta\Omega - \eta s\lambda_v|$ should be satisfied. Thus, $\Delta\Omega$ should satisfy the condition $2s\lambda_v - E_F - \Delta < \Delta\Omega < E_F - \Delta$ for the $K$ valley and $\Delta - E_F < \Delta\Omega < E_F + \Delta + 2s\lambda_v$ for the $K'$ valley. Generally, for monolayer TMDc materials, $\lambda_v$ is much smaller than $\Delta$, therefore, the range of $\Delta$ can be simplified as $\Delta - E_F < \Omega < E_F - \Delta$. When the absolute value of $\Delta\Omega_0$ goes beyond $E_F - \Delta$, the electronic transport become totally $K$ polarized or $K'$ polarized due to optical Stark effect. In the PH configuration, the energy-band shift induced by CPL are the same in regions I and II, $\Delta\Omega_I = \Delta\Omega_{II} = \Delta\Omega_0$. The valley-polarized energy windows are $\Delta\Omega_0 < \Delta - E_F$ for $K$ polarization and $\Delta\Omega_0 > E_F - \Delta$ for $K'$ polarization [see Figs. 6(a) and 6(b)]. However, such valley-polarized energy windows do not exist in the APH configuration, where the energy shift caused by optical Stark effect is opposite in regions I and II, $\Delta\Omega_I = -\Delta\Omega_{II} = \Delta\Omega_0$. When $\Delta\Omega_0 < \Delta - E_F$, the $K$ polarized particles that transport through region I are blocked in region II, therefore, no particles may contribute to electronic transport within this energy window. And the same result is gained in the case $\Delta\Omega_0 > E_F - \Delta$ [see Figs. 6(c) and 6(d)]. This conclusion well explains why total conductance rapidly decays to zero in the APH configuration

shown in Fig. 4(a). It also implies that $E_F - \Delta$ can be a good estimation of $\Delta\Omega_0$ limit to achieve 100% TOR (the deviation from calculation results in Fig. 4(a) is less than 0.1 eV).

## IV. CONCLUSION

In summary, we have studied both spin- and valley-resolved electronic transport properties of the double-beam CPL-modulated quantum structure. Significant differences in total conductance can be found between PH and APH configurations in CPL-modulated structures, which quite resembles the TMR effect observed in FNF junctions. However, numerical results of spin- and valley-resolved transmission and conductance show an inconsistent origin of tunneling resistance. We name the tunneling resistance effect observed in CPL modulated quantum structures as the tunneling optoresistance effect, and subsequently introduce ratio TOR to describe such a quantum effect. Calculation results imply that TOR = 1 can be realized when the CPL-induced gap is beyond a certain limit. We give an intuitive explanation near $K$ and $K'$ valleys, together with an evaluation of $\Delta\Omega_0$ limit for junctions based on different TMDc materials to achieve TOR = 1.

For CPL-modulated quantum structures, we propose that high resistance and low resistance can be achieved only by optical pumping, thus the conversion between two configurations can be dynamically controlled, which cannot be achieved in models of magnetic modulation. This work reveals that CPL-modulated quantum structures based on monolayer TMDc have promising potential for applications in high-speed spintronic and valleytronic devices.

The data that support the findings of this study are available from the corresponding author upon reasonable request.

## ACKNOWLEDGMENTS

This work was supported by the National Natural Science Foundation of China (Grant No. 12074209).

[1] A. Avsar, H. Ochoa, F. Guinea, B. Özyilmaz, B. J. van Wees, and I. J. Vera-Marun, Rev. Mod. Phys. **92**, 021003 (2020).
[2] C. Park, Phys. Rev. Appl. **11**, 044033 (2019).
[3] K. Zollner, P. E. F. Junior, and J. Fabian, Phys. Rev. B **100**, 195126 (2019).
[4] Y. Liu, Y. Gao, S. Zhang, J. He, J. Yu, and Z. Liu, Nano Res. **12**, 2695 (2019).
[5] K. F. Mak, C. Lee, J. Hone, J. Shan, and T. F. Heinz, Phys. Rev. Lett. **105**, 136805 (2010).
[6] P. Yang, X. Zou, Z. Zhang, M. Hong, J. Shi, S. Chen, J. Shu, L. Zhao, S. Jiang, X. Zhou, Y. Huan, C. Xie, P. Gao, Q. Chen, Q. Zhang, Z. Liu, and Y. Zhang, Nat. Commun. **9**, 979 (2018).
[7] H. Li, J. Wu, Z. Yin, and H. Zhang, Acc. Chem. Res. **47**, 1067 (2014).
[8] B. Liu, M. Fathi, L. Chen, A. Abbas, Y. Ma, and C. Zhou, ACS Nano **9**, 6119 (2015).
[9] D. Kong, H. Wang, J. J. Cha, M. Pasta, K. J. Koski, J. Yao, and Y. Cui, Nano Lett. **13**, 1341 (2013).
[10] Y. Chang, W. Zhang, Y. Zhu, Y. Han, J. Pu, J. K. Chang, W. T. Hsu, J. K. Huang, C. L. Hsu, M. H. Chiu, T. Takenobu, H. Li, C. I. Wu, W. H. Chang, A. T. S. Wee, and L. J. Li, ACS Nano **8**, 8582 (2014).
[11] S. Barraza-Lopez, B. M. Fregoso, J. W. Villanova, S. S. P. Parkin, and K. Chang, Rev. Mod. Phys. **93**, 011001 (2021).
[12] W.-T. Lu, H.-Y. Tian, H.-M. Liu, Y.-F. Li, and W. Li, Phys. Rev. B **98**, 075405 (2018).
[13] Y. Hajati, M. Alipourzadeh, and I. Makhfudz, Phys. Rev. B **104**, 205402 (2021).
[14] D. N. Liu, B. Y. Liu, R. Y. Yuan, J. Zheng, and Y. Guo, Phys. Rev. B **103**, 245432 (2021).
[15] H. Rostami and R. Asgari, Phys. Rev. B **91**, 075433 (2015).
[16] Y. C. Cheng, Q. Y. Zhang, and U. Schwingenschlögl, Phys. Rev. B **89**, 155429 (2014).
[17] H. Li, J. Shao, D. Yao, and G. Yang, ACS Appl. Mater. Interfaces **6**, 1759 (2014).
[18] A. T. Hanbicki, G. Kioseoglou, M. Currie, C. S. Hellberg, K. M. McCreary, A. L. Friedman, and B. T. Jonker, Sci. Rep. **6**, 18885 (2016).
[19] X. Song, S. Xie, K. Kang, J. Park, and V. Sih, Nano Lett. **16**, 5010 (2016).
[20] A. M. Jones, H. Yu, J. S. Ross, P. Klement, N. J. Ghimire, J. Yan, D. G. Mandrus, W. Yao, and X. Xu, Nat. Phys. **10**, 130 (2014).
[21] H.-Z. Lu, W. Yao, D. Xiao, and S.-Q. Shen, Phys. Rev. Lett. **110**, 016806 (2013).
[22] R. Bertoni, C. W. Nicholson, L. Waldecker, H. Hübener, C. Monney, U. De Giovannini, M. Puppin, M. Hoesch, E. Springate, R. T. Chapman, C. Cacho, M. Wolf, A. Rubio, and R. Ernstorfer, Phys. Rev. Lett. **117**, 277201 (2016).
[23] J. S. Moodera, L. R. Kinder, T. M. Wong, and R. Meservey, Phys. Rev. Lett. **74**, 3273 (1995).
[24] J. Mathon and A. Umerski, Phys. Rev. B **63**, 220403(R) (2001).
[25] W. H. Butler, Sci. Tech. Adv. Mater. **9**, 014106 (2008).
[26] H. Maehara, K. Nishimura, Y. Nagamine, K. Tsunekawa, T. Seki, H. Kubota, A. Fukushima, K. Yakushiji, K. Ando, and S. Yuasa, Appl. Phys. Express **4**, 033002 (2011).
[27] F. Zhai and K. Chang, Phys. Rev. B **77**, 113409 (2008).
[28] O. Oubram, O. Navarro, E. J. Guzmán, and I. Rodríguez-Vargas, Superlattices Microstruct. **113**, 483 (2018).
[29] R. Saxena, A. Saha, and S. Rao, Phys. Rev. B **92**, 245412 (2015).
[30] T. Yokoyama, Phys. Rev. B **87**, 241409(R) (2013).
[31] D. Wang and G. Jin, Phys. Lett. A **378**, 2557 (2014).
[32] S. Rachel and M. Ezawa, Phys. Rev. B **89**, 195303 (2014).
[33] H. Wang, X. Chen, B. Zhou, W. Liao, and G. Zhou, Physica B (Amsterdam, Neth.) **406**, 4407 (2011).
[34] J. Zou, G. Jin, and Y. Ma, J. Phys.: Condens. Matter **21**, 126001 (2009).
[35] Y. Hajati, M. Alipourzadeh, and I. Makhfudz, Phys. Rev. B **103**, 245435 (2021).
[36] C. Zhao, J. Ou, Z. Wen, and W. Lu, Phys. Lett. A **452**, 128443 (2022).
[37] J. G. Rojas Briseño, M. A. Flores Carranza, P. Villasana Mercado, S. Molina Valdovinos, and I. Rodríguez Vargas, Phys. Rev. B **103**, 155431 (2021).

[38] D. Wang, Z. Huang, Y. Zhang, and G. Jin, Phys. Rev. B **93**, 195425 (2016).
[39] X. Qiu, Z. Cao, J. Hou, and C. Yang, Appl. Phys. Lett. **117**, 102401 (2020).
[40] K. F. Mak, K. He, J. Shan, and T. F. Heinz, Nat. Nanotechnol. **7**, 494 (2012).
[41] H. Zeng, J. Dai, W. Yao, D. Xiao, and X. Cui, Nat. Nanotechnol. **7**, 490 (2012).
[42] M. Khezerlou and H. Goudarzi, Superlattices Microstruct. **86**, 243 (2015).
[43] D. Xiao, G. Liu, W. Feng, X. Xu, and W. Yao, Phys. Rev. Lett. **108**, 196802 (2012).
[44] T. Kitagawa, T. Oka, A. Brataas, L. Fu, and E. Demler, Phys. Rev. B **84**, 235108 (2011).
[45] M. Büttiker, Phys. Rev. Lett. **57**, 1761 (1986).